Encapsulation of nano-Si into MOF glass to enhance lithium-ion battery anode performances

Yan, Jiajia; Gao, Chengwei; Qi, Shibin; jiang, zhenjing; Jensen, Lars Rosgaard; Zhan, Hongbing; Zhang, Yanfei; Yue, Yuanzheng

Link to publication from Aalborg University

Encapsulation of nano-Si into MOF glass to enhance lithium-ion battery anode performances

Jiajia Yan [a],[1], Chengwei Gao [b],[1], Shibin Qi [c], Zhenjing Jiang [c],[d], Lars Rosgaard Jensen [e], Hongbing Zhan [f], Yanfei Zhang [c],[*], Yuanzheng Yue [a],[*]

[a] Department of Chemistry and Bioscience, Aalborg University, DK-9220 Aalborg, Denmark
[b] Laboratory of Infrared Material and Devices, Advanced Technology Research Institute, Ningbo University, Ningbo 315211, China
[c] School of Materials Science and Engineering, Qilu University of Technology (Shandong Academy of Sciences), Jinan 250353, China
[d] SEU-FEI Nano-Pico Center, Key Laboratory of MEMS of Ministry of Education, Southeast University, Nanjing 210096, China
[e] Department of Materials and Production, Aalborg University, 9220 Aalborg, Denmark
[f] College of Materials Science and Engineering, Fuzhou University, Fuzhou 350108, China

ABSTRACT

Although metal-organic framework (MOF) glasses have exhibited high potential to be applied as anode materials for lithium-ion batteries (LIBs), their electrochemical performances still need to be greatly improved to match the rapid development of green energy technologies. Silicon is a promising candidate for the next generation of LIB anode but suffers from vast volume fluctuations upon lithiation/delithiation. Here, we present a strategy to in situ grow a kind of MOF, namely, cobalt-ZIF-62 ($Co(imidazole)_{1.75}(benzimidazole)_{0.25}$) on the surface of Si nano particles, and then to transform the thus-derived material into Si@ZIF-glass composite (SiZGC) through melt-quenching. The robust hierarchical structure of the SiZGC based anode exhibits the specific capacity of ~650 mA h g^{-1}, which is about three times that of pure ZIF glass and about six times that of pristine ZIF crystal at 1 A g^{-1} after 500 cycles. The origin of this huge enhancement is revealed by performing structural analyses. The ZIF glass phase can not only contribute to lithium storage, but also buffer the volume changes and prevent the aggregation of Si nano particles during lithiation/delithiation processes.

1. Introduction

Lithium-ion batteries (LIBs) are still the main energy storage devices to meet the demand for clean and sustainable energy. The anode material in commercial LIBs is primarily graphite, which can accommodate lithium ions and exhibit a theoretical gravimetric capacity of 372 mA h g^{-1} [1]. However, the capacity of graphite cannot meet the market demand for large-scale applications with high energy/power density and operation reliability. Therefore, it is vital to develop new anode materials with high capacity, low charging/discharging potential, and low production cost.

Concerning the specific capacity, silicon (Si) is potentially the best alternative anode material for LIBs, as it has a theoretical specific capacity of > 4000 mA h g^{-1}. In addition, Si is non-toxic and is the second most abundant element in earth crust, exhibiting low average discharge potential vs. Li$^+$/Li. However, pure Si anode exhibits very poor cycling

stability, i.e., capacity retention is only about 50 mA h g^{-1} within 100 cycles [2,3] due to the enormous volumetric expansion (> 300%) upon lithiation [4]. Furthermore, the low intrinsic electronic conductivity of Si leads to the sluggish electrochemical kinetics and causes severe polarization, limiting the utilization of Si anodes. To solve the aforementioned critical problems, significant efforts have been devoted to modifying Si morphology in nanoscale [5] and compositing Si with conducting and/or stress-relief buffer matrix to accommodate volume expansion [5–7]. For example, Cui et al. reported a silicon-nanolayer-embedded graphite anode for LIBs [8]. Thus, a delicate structure design based on Si for anode material is necessary to achieve outstanding battery performances.

Metal-organic frameworks (MOFs), which are three-dimensional networks constructed by metal nodes and organic ligands, have been receiving much attention owing to their promising applications, e.g., in catalyst, drug delivery, energy harvest, conversion and storage.

Considering the ultrahigh specific surface area for contacting with collector, abundant active sites for Li$^+$ ions storage, as well as the tunable pores for migration of the Li$^+$ ions, MOFs are regarded as one of the most potential candidates to replace current graphite anode for LIBs [9,10]. Crystalline MOF-177, first used as anode materials by Chen et al. shows a high irreversible initial capacity of 400 mA h g^{-1} but low capacity of 100 mA h g^{-1} after 2 discharging/charging cycles [10]. To tackle the problem of poor electronic conductivity of MOF anodes, MOFs are coated with graphene to obtain the MOF/graphene composite anode, and thereby deliver a reversible capacity up to ~1075 mA h g^{-1} at a current density of 50 mA g^{-1} [11] and 400 mA h g^{-1} at the current density of 100 mA g^{-1} [9]. However, their reversible capacities at higher current densities still need further improvement to meet the soaring demands from modern electronic devices and electric vehicles.

As a promising method for improving the performances of anodes, vitrification of MOFs provides additional channels for Li$^+$ ion diffusion and storage due to the increased distortion and local breakage of the Co-N coordination bonds. Note that zeolitic imidazolate frameworks (ZIFs) are a subset of MOFs. It was recently reported that the anode based on cobalt-ZIF-62 glass exhibits high lithium storage capacity, i.e., 306 mA h g^{-1} after 1000 cycles at 2 A g^{-1}, high cycling stability, and superior rate performance compared with both crystalline and amorphous ones (prepared by high-energy ball-milling) [12]. It should be mentioned that cobalt-ZIF-62 is a type of ZIF with the composition of Co(imidazole)$_{1.75}$(benzimidazole)$_{0.25}$. However, the ZIF glass anode still faces a main challenge, e.g., the limited reversible capacity. This inspired us to fabricate composite by combing the advantages of MOF glass and high-capacity Si materials to obtain high-performance anodes.

Recent progress in developing Si@MOF composite has dramatically enlarged the design space for anode materials [13–16]. Although crystalline MOFs have been utilized in fabricating the Si@MOF composites, the glassy MOF/Si composites have not been reported to the best of our knowledge [13,14]. In this work, we first applied a reflux technique (see Experimental section) to prepare Si nano particles@cobalt-ZIF-62 composites. Then we heated them to 450 °C, at which cobalt-ZIF-62 was melted and subsequently quenched to glass state, and thus the Si@calbolt-ZIF-62-glass composites (SiZGC) were obtained. This fabrication process involves wrapping Si nano particles into ZIF-62 and melt quenching treatment. We chose ZIF-62 as the precursor since it can be easily melt-quenched to glass state with a disordered open network, benefiting to the Li-ion storage and transfer [12,17,18]. Si nano-particles increased the yield of ZIF-62 by providing heterogeneous nucleation sites for ZIF crystal formation. Thus, a synergistic effect was achieved for the composite-based anode, which led to a rather high reversible capacity (650 mA h g^{-1} at 1 A g^{-1} after 500 cycles). This capacity is about 3 times higher than that of ZIF glass, 6 times that of ZIF crystal, and 30 times that of pure Si-based anodes. The strategy used in this work not only buffered the volume expansion and the aggregation of Si nano particles during cycling, but also made full use of ZIF-62 glass for lithium storage. We clarified the structural origin of the enhancement of the capacity in the derived composite-based anodes.

2. Experimental section

2.1. Synthesis of samples

Cobalt-ZIF-62 crystal (Z) was synthesized by conventional solvothermal method [18–20]. The cobalt-ZIF-62 glass (ZG) was obtained by heating the Z at 10 °C·min^{-1} in argon to 450 °C and calcined at this temperature for 5 mins followed by cooling naturally to room temperature [12]. Instead of using the solvothermal method, Si@cobalt-ZIF-62 composite (SiZC) was prepared via a reflux method, which involves: 1) heating the chemically reacting solution for a period at a certain temperature; 2) condensing the vapor to liquid state via a pipe. In detail, imidazole (Im, 11.55 mmol, 785.4 mg), benzimidazole (BIm, 1.66 mmol, 196 mg), C$_4$H$_6$CoO$_4$•4H$_2$O (4 mmol, 996 mg), and Si

nanoparticles with different amounts (50, 100, 150 mg, accounting for about 5%, 10%, 15 wt% of the final product, respectively), were added to 90 mL *N,N*-dimethylformamide (DMF). Then the solution was heated at 130 °C for 48 hrs while refluxing and stirring. After cooling naturally to room temperature, the SiZC was obtained by centrifugation and vacuum drying. The SiZC was melt-quenched using the same procedure as that vitrifying the Z to obtain Si@cobalt-ZIF-62-glass composite (SiZGC), in which Si remains crystalline. The samples are named according to the weight percentage of Si in composite. For example, 5SiZGC refers to the SiZGC containing 5 wt% Si. The detailed preparation procedures are given in Table 1.

2.2. Materials characterizations

The phases of the samples were identified on a PANalytical X-ray diffractometer with Cu Kα (λ = 1.5406 Å) radiation during the 2θ range of 5–70° with a step size of 0.013°. To investigate the characteristic temperature of glassy material, i.e., glass-transition temperature, the differential scanning calorimeter (DSC) (Jupiter 449 C, Netzsch) measurements were conducted at 10 °C·min^{-1} in argon to 450 °C. The Raman spectroscopy measurements were conducted via Renishaw In-Via Raman microscopic with an Ar$^+$ laser (λ = 532 nm). Fourier transform infrared (FTIR) spectra were recorded on a Bruker TENSOR II FTIR spectrometer with Platinum ATR Accessory at room temperature in the range of 400–4000 cm^{-1}. To study the chemical environment of Co, Si, C, N, O in anodes before and after discharging/charging cycling, X-ray photoelectron spectroscopy (XPS) measurements were performed using ESCALAB 250Xi spectrometer (ThermoFisher Scientific, USA) with nonmonochromatic Al Ka X-ray (1486.6 eV) at pass energy of 50 eV. The morphologies and element distributions of samples were analyzed using field-emission scanning electron microscopy (FE-SEM) (Supra-55, Zeiss Inc.), transmission electron microscopy (TEM) (JEOL Ltd., Japan) and X-ray energy dispersive spectroscopy (EDS) (X-Max, OXFORD Instruments Inc.).

2.3. Cell assembly and electrochemical evaluation

The electrochemical performances of the obtained samples were evaluated by using CR2032 coin cells with lithium foil (diameter of 10.0 mm) as the counter/reference electrode. A uniform slurry consisting of 70 wt% active materials (the as-prepared ZIFs or Si@ZIFs), 20 wt% acetylene black, and 10 wt% polyvinylidene difluorides (PVDF) were prepared in N-methyl-2-pyrrolidone (NMP) and then pasted onto a copper foil substrate via a doctor blade and dried at 110 °C in a vacuum oven for 12 h to obtain working electrodes. The loading amount of active materials was 1~2 mg. 1 M LiPF$_6$ in ethylene carbonate (EC)/diethyl carbonate (DEC)/dimethyl carbonate (DMC) (1:1:1 vol%) and a Celgard 2325 membrane (diameter of 19.0 mm) were used as the electrolyte and separator, respectively. The cells were assembled in an argon-filled glovebox with both the moisture and the oxygen content lower than 0.1 ppm and then the cells were tested at 25 °C. The galvanostatic charging/discharging tests of the samples were conducted on a Land battery test system (CT2001A) within the voltage range 0.01–3 V. Cyclic voltammetry (CV) curves were obtained in the voltage range of 0.01–3 V

Table 1
The preparation procedures of the cobalt-ZIF-62 crystal (Z), cobalt-ZIF-62 glass (ZG), Si@cobalt-ZIF-62 composite (SiZC), and Si@cobalt-ZIF-62-glass composite (SiZGC).

Sample Names	Preparation Procedures		Melt-Quenching
	Solvothermal	Reflux	
Z	√	–	–
ZG	√	–	√
SiZC	–	√	–
SiZGC	–	√	√

at the scanning rate of 0.1 mV s^{-1}. EIS spectra were recorded in the frequency range of 0.1 Hz–100 kHz on CHI 760e electrochemical workstation. All electrochemical measurements were repeated with different batches of samples to confirm the reproducibility of their performances.

3. Results and discussion

Scheme 1 illustrates the fabrication process of the Si@cobalt-ZIF-62-glass composite (SiZGC). First, the raw materials including organic ligand, metal ions, and Si nano-powder, were dispersed in the DMF, and then reflux at 130 °C for 2 days to precipitate the Si@ZIF-62 composite (SiZC) (see Experimental section). The Si nanoparticles act as hetero-nucleation sites for growing ZIF layer. Second, the obtained SiZC was heated to 450 °C at 10 °C·min^{-1} in argon and then cooled down naturally, leading to the SiZGC formation. Finally, Si nanoparticles with a size distribution of 20~60 nm were encapsulated in ZIF glass matrix, resulting in a robust structure that buffers the volume changes of Si during lithiation/delithiation processes.

The morphologies and microstructures of samples 10SiZC and 10SiZGC were examined using field emission scanning electron microscopy (FE-SEM), as shown in Fig. 1. For 10SiZC (Fig. 1a), ZIF particles with a size of ~10 μm are observed, in which Si nanoparticles are wrapped, as verified by EDS elemental mappings of Co, N, and Si. Thus, SiZC was obtained by the facile reflux method. The SEM image of 10SiZGC (Fig. 1b) reveals that the ZIF cages remain owing to the high viscosity of ZIF melt, and hence, the morphologies of 10SiZGC are similar to those of 10SiZC. In addition, the enlarged image (Fig. 1b) indicates that small Si particles are covered by ZIF-62 glass.

To obtain the crystallographic information on the studied samples, X-ray diffraction (XRD) measurements were conducted (Fig. 2a). In the XRD patterns of Z and 10SiZC, sharp diffraction peaks can be seen in the range of 10°~25°, coinciding with those in the simulated ZIF-62 [12]. Moreover, the Bragg diffraction peaks associated with Si were also observed in 10SiZC, further confirming the wrapping of nano Si particles by crystalline ZIF-62. In contrast, the XRD patterns of sample ZG show no diffraction peaks, indicating its amorphous nature. While the diffraction peaks for Si crystals also appear in the XRD pattern of 10SiZGC sample. Thus, ZIF-62 becomes amorphous while Si remains crystalline in 10SiZGC upon melt-quenching. That is, the melt-quenching method did not affect the crystal structure of Si.

Fig. 2b shows the DSC upscan curves of Z, ZG, 10SiZC and 10SiZGC samples obtained at 10 °C min^{-1} in argon. For both Z and 10SiZC, the DSC curve of each sample exhibits an endothermic peak at around 280 °C due to the release of solvent, followed by another endothermic peak at 420 °C associated with the melting event. However, a different scenario is observed for both ZG and 10SiZGC samples, i.e., the glass transition occurs at ~330 °C, implying that the vitrification of ZIF in

10SiZC is not affected by introducing Si. To evaluate the thermal stability, thermogravimetry (TG) curves of Z, ZG, 10SiZC, and 10SiZGC were collected. As shown in Fig. S1, significant mass loss occurs in both Z and 10SiZC in the temperature range of 150–300 °C owing to the solvent (DMF) release, while no mass loss is seen in both ZG and 10SiZGC as the solvent was already released during the glass preparation process.

The FTIR spectra of Z, ZG, 10SiZC and 10SiZGC in Fig. 2c show the similar frequencies of intramolecular vibrations, indicating that the integrity of organic linkers in ZIFs are preserved during melt-quenching [19]. However, structural changes take place during transformation of crystal into glass (Fig. 2c). First, the peaks at around 430 and 835 cm^{-1} correspond to Co-N bonds and the in-plane bending of aromatic rings, respectively [12,21], and both peaks shift to a lower wavenumber after vitrification, suggesting that both Co-N bonds and aromatic rings become weaker in ZG and 10SiZGC. Second, the intensity ratio between the 668 and 1082 cm^{-1} peaks increases and the two peaks are attributed to the ring deformation out-of-plane-bending in the organic ligands and the C-H bending vibrations, respectively [12]. This implies an increased distortion in glass samples. Third, the peaks at 1383 and 1675 cm^{-1} arising from vibrational mode of C-H and the carbonyl groups of solvent molecules (DMF) disappear upon vitrification [12,22]. This indicates that the DMF molecules have escaped from Z or 10SiZC during melt-quenching, agreeing with the DSC results. It is worth noting that the Si-Si bonds were not detected in FTIR spectra for 10SiZC and 10SiZGC since Si is FTIR-inactive. However, the strong peak at ~517 cm^{-1} assigned to Si-Si bonds [23] was observed in Raman spectra (Fig. 2d) for those two samples, verifying the existence of Si in the target composites.

To evaluate the anode performances of the Si@ZIF composites, the cycling experiments of the commercial nano-Si, Z, ZG, 5SiZC, 5SiZGC, 10SiZC, 10SiZGC, 15SiZC, and 15SiZGC based anodes were performed at a current density of 1 A g^{-1} (Fig. 3a). The specific capacity of almost every sample decays distinctly within about 50 cycles and then increases dramatically, except for the Si and Z based anodes which deliver rather low capacities. Specifically, the Si-doped composite samples exhibit remarkably higher capacities than those of the corresponding pure ZIF-crystal/glass and Si. This implies that the co-existence of ZIF layer and Si leads to a synergistic effect that benefits both Li-ion storage and transport. Specifically, the ZIF layer can protect Si from pulverization by buffering the volume changes during charging/discharging cycles, while Si provides large specific capacity. In addition, the ZIF glass-containing composites show higher capacities than the samples with ZIF crystal, except for the samples doped with 15 wt% Si. The capacity of 650 mA h g^{-1} of 10SiZGC based anode can be reached at 1 A g^{-1} after 500 cycles, i.e., it is more than three times that of ZG (210 mA h g^{-1}), six times that of pristine ZIF crystal (108 mA h g^{-1}), and 30 times that of pure Si (20 mA h g^{-1}). This is a remarkable enhancement, considering that the specific capacities are calculated based on the mass of the total
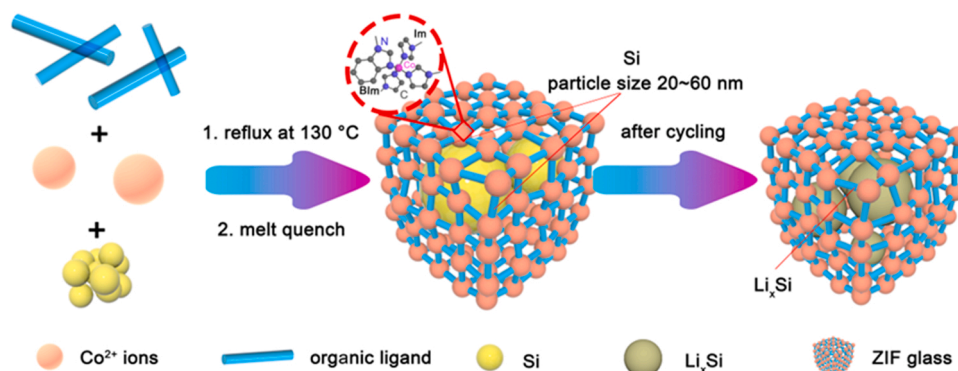
Scheme 1. Schematic illustration of the synthesis process of the Si@cobalt-ZIF-62-glass composite (SiZGC) and the protecting role of ZIF glass matrix, which prolongs the cycling life of Si.
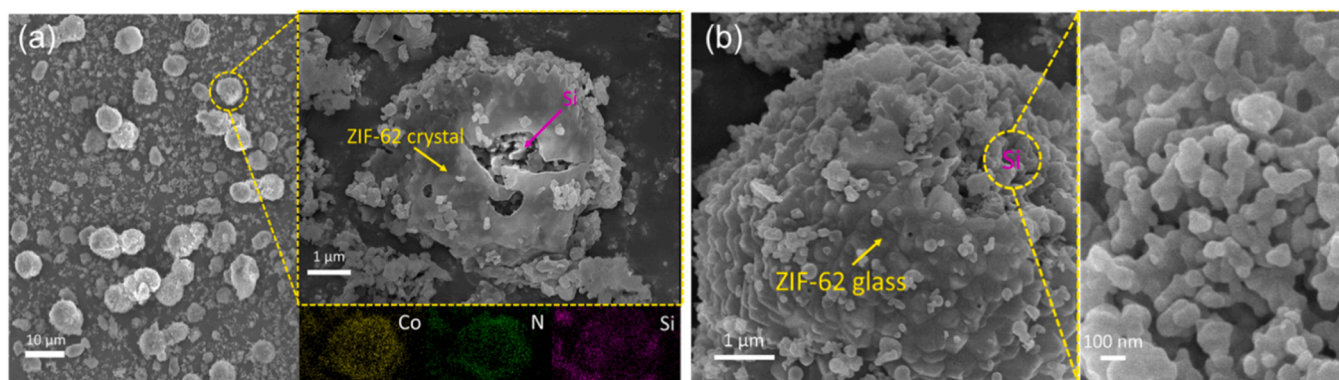
Fig. 1. Microscopic characterizations. (a) SEM images of the 10Si@cobalt-ZIF-62 composite (10SiZC) (Inset: EDS elemental mappings of Co, N and Si for SZ), where the number, i.e., 10, represents the introduction of 10 wt% Si nanoparticles into ZIF-62; (b) SEM images of the 10Si@cobalt-ZIF-62-glass composite (10SiZGC).
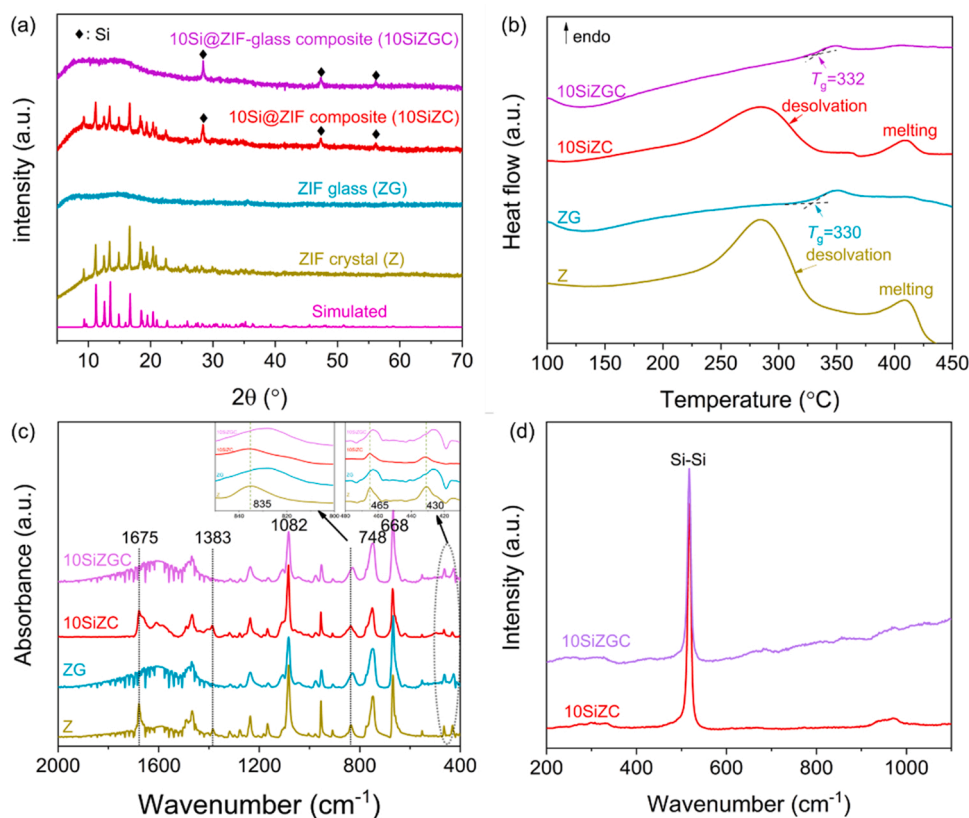

Fig. 2. Phase, thermal and structure analyses of the ZIF crystal (Z), ZIF glass (ZG), 10Si@ZIF composite (10SiZC), and 10Si@ZIF-glass composite (10SiZGC). (a) XRD patterns along with that of simulated ZIF-62. (b) DSC upscan curves which were obtained at 10 °C min^{-1} in argon. (c) FTIR spectra. (d) Raman spectra of 10SiZC and 10SiZGC.

active material - Si@ZIF composite, and only ~10 wt% of Si exists in the active material for 10SiZGC. This means that 10 wt%Si contributes around 400 mA h g^{-1} to the total capacity, which almost reaches the theoretical capacity of 10%Si as that of pure Si is ~4000 mA h g^{-1}. In addition, 10SiZC and 5SiZGC also show high capacities, reaching 600 and 550 mA h g^{-1} after 500 cycles at 1 A g^{-1}, respectively. All these results not only suggest that the Si@ZIF composite exhibits a synergistic effect (i.e., a combination of high capacity and high cycling stability) compared with pure Si and ZIFs [2,12], but also indicate the important role of ZIF glass in protecting Si in the composite. Fig. S2 shows the cycling performance of 10SiZGC after 1000 cycles at 1 A g^{-1}. Apparently, the capacity of 10SiZGC did not rise all the way but peaked at 660 mA h g^{-1} after 570 cycles and then declined to 450 mA h g^{-1} after

1000 cycles. This could be attributed to structural evolution of ZIF and the pulverization of Si during lithiation/delithiation.

To probe the electrochemical performances of 5SiZC, 10SiZC, 15SiZC, 5SiZGC, 10SiZGC, and 15SiZGC samples, we also investigated their rate capabilities (Fig. 3b). The results suggest the excellent kinetics of the SiZGC-based anodes at different current densities up to 5 A g^{-1}. As expected, 15SiZGC, 10SiZGC, and 5SiZGC manifested outstanding high-rate capability compared with other samples, delivering the favorable average capacities of 666, 516, and 482 mA h g^{-1} after 10 cycles at 0.1 A g^{-1}, respectively. This can be explained in terms of the amounts of doping Si and the effects of ZIF glass. The glass phase provides more Li-ion intercalation sites arising from increased distortion and defects compared with crystalline ZIF [12]. With a stepwise increase in the
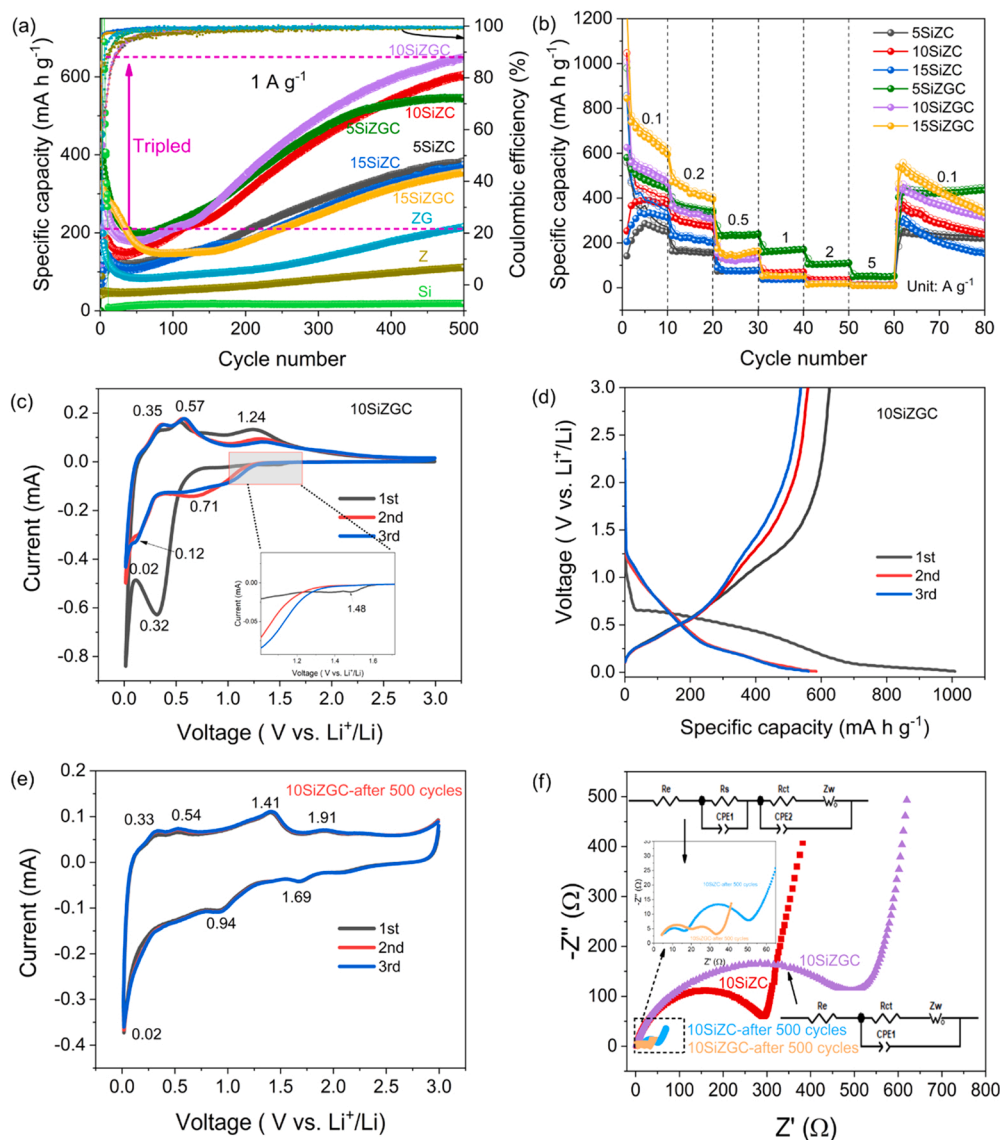
Fig. 3. Electrochemical Performances. (a) The cycling performance of anodes based on the ZIF crystal (Z), ZIF glass (ZG), 5Si@ZIF composite (5SiZC), 5Si@ZIF-glass composite (5SiZGC), 10Si@ZIF composite (10SiZC), 10Si@ZIF-glass composite (10SiZGC), 15Si@ZIF composite (15SiZC), 15Si@ZIF-glass composite (15SiZGC), where the numbers, i.e., 5, 10, 15, represent that weight percent of Si nanoparticles introduced into ZIF-62, respectively, at 1 A g^{-1} for 500 cycles. (b) Rate performance of 5SiZC, 5SiZGC, 10SiZC, 10SiZGC, 15SiZC, and 15SiZGC at current densities of 0.1, 0.2, 0.5, 1, 2, 5 and 0.1 A g^{-1}. (c) Cyclic Voltammetry (CV) curves of pristine 10SiZGC within the range from 0.01 to 3.0 V at a scan rate of 0.1 mV s^{-1}. (d) Galvanostatic charge-discharge voltage profiles of 10SiZGC for three cycles at the current density of 0.1 A g^{-1}. (e) Cyclic Voltammetry (CV) curves of 10SiZGC after 500 cycles within the range from 0.01 to 3.0 V at a scan rate of 0.1 mV s^{-1}. (f) Nyquist plots of 10SiZC and 10SiZGC before and after cycling obtained from electrochemical impedance spectra within frequency range from 0.01 Hz to 100 kHz.

current density, the average capacity decreases for all the samples, among which 5SiZGC exhibits the highest capacity retention after cycles at 0.5, 1, 2, and 5 A g^{-1}. In addition, when the current density was set back to 0.1 A g^{-1}, the specific capacity of 5SiZGC can recover to 432 mA h g^{-1} and remains stable in the following cycles, indicating a superior rate performance. In contrast, both 15SiZGC and 10SiZGC are sensitive to the current density and show a rapid decline in capacity retention rate with an increase of the current density. When the current density was switched back to 0.1 A g^{-1}, the capacities of 15SiZGC and 10SiZGC restore to 540 and 440 mA h g^{-1}, respectively, and decrease slowly in the following cycles. This could be explained as follows. Although the Si content in 15SiZGC and 10SiZGC is higher than that in 5SiZGC, not all the Si nanoparticles in the composite contributed to the capacity increase within the studied 80 cycles in the test of rate capability. When introducing more Si into the composite, e.g., 10SiZGC, the glassy ZIF cages simply cannot accommodate all Si, as shown in Fig. 1a. The additional Si particles will aggregate and collapse during lithiation/delithiation because no ZIF protection layer exists, resulting in a capacity decline.

The cyclic voltammetry (CV) measurements of 10SiZGC at a scan rate of 0.1 mV s^{-1} were carried out to investigate the electrochemical reaction, as shown in Fig. 3c. In the first cathodic scan, there are three

distinct reduction peaks at around 1.48, 0.32, and 0.02 V, which are attributed to the storage of Li$^+$ within ZIF, formation of solid electrolyte interface film (SEI), and formation of Li$_x$Si phase, respectively [24–27]. During the anodic reaction, the peaks at around 0.35 and 0.57 V are ascribed to dealloying of Li$_x$Si to Si, while the peak at ~1.23 V comes from the extraction of Li$^+$ from ZIF glass [12,27]. In the subsequent two CV curves, the pair of redox peaks (~0.71 versus ~1.24 V) arises from reversible insertion or extraction of Li$^+$ into/from ZIF glass, whereas both the 0.12 vs 0.57 V pair and the 0.02 vs 0.35 V pair are associated with the alloying-dealloying processes of Si/Li$_x$Si [28]. Fig. 3d shows the typical galvanostatic discharge/charge voltage profiles in the first three cycles of 10SiZGC anode at 0.1 A g^{-1}. The observed plateau voltage in the profiles is consistent with the peak voltage in the CV curves. The initial discharge and charge capacities were 1010 and 627 mA h g^{-1}, respectively, giving the first Coulombic efficiency of 62%, and the irreversible capacity loss may be due to the formation of the SEI layer and other irreversible reactions [29].

To clarify why the capacity of 10SiZGC continuously increases during 500 cycles, three CV cycling of 10SiZGC after 500 charging/discharging cycles were performed (Fig. 3e). Remarkably, compared with the redox peaks in the CV profiles of the fresh battery (Fig. 3c), a new couple of redox peaks appear, i.e., (1.69 vs 1.91 V), which can be

ascribed to the reversible insertion/extraction of Li$^+$ into/from ZIF glass [30]. This indicates that the ZIF glass is gradually activated for lithium storage as a result of the charging/discharging cycling, which contributed to the enhancement of the capacity. Moreover, the redox peaks located at ~0.71 and ~1.24 V in Fig. 3c shift to higher voltages, i.e., ~0.94 and ~1.41 V (Fig. 3e). The peak at 0.12 V in the second cathodic curve in Fig. 3c does not appear in Fig. 3e, implying the gradual structural changes in both ZIF glass and Si with cycling. In addition, the overlapping of three CV curves in Fig. 3e indicates the reversibility of 10SiZGC after 500 cycles.

To understand the origin of the electrochemical performance enhancement in 10SiZGC upon cycling, the electrochemical impedance spectroscopy (EIS) measurements of 10SiZC and 10SiZGC before and after 500 cycles were performed (Fig. 3 f). All the Nyquist plots consist of one or two depressed semicircles in the high frequency region and an inclined line in the low frequency region. The equivalent circuit for the Nyquist plots is given in the inset of Fig. 3 f, where R_e, R_s, R_{ct}, C_{PE} and Z_w

represent the ohmic resistance, SEI resistance, charge transfer resistance, interface capacitance and diffusion impedance of the half-cell systems, respectively [12,29]. The fitted parameters are shown in Table S1. It is seen that the charge transfer resistance (R_{ct}) of 10SiZC and 10SiZGC decreases from 290.4 and 405.3 Ω to 29.7 and 10.8 Ω after 500 cycles, respectively, indicating the increased electrical conductivity. In addition, the depressed semicircle in each EIS curve of 10SiZC and 10SiZGC splits into two consecutive ones after cycling. The semicircle in the higher frequency region arises from the SEI impedance (R_s and C_{PE1}). The line inclined at approximately 45° in the low frequency region corresponds to the Warburg impedance (W), which is associated with the diffusion coefficient of Li$^+$ in the electrode material. Warburg factor (σ) can be determined from the linear relation between impedance Z′ and the reciprocal square root of the angular frequency ω (Fig. S3). As shown in Fig. S3, the σ values of 10SiZC and 10SiZGC before and after cycling are 191.78, 320.88, 32.36, and 14.16, respectively. The declined σ value after cycles suggests a larger Li$^+$ diffusion coefficient [12,31].
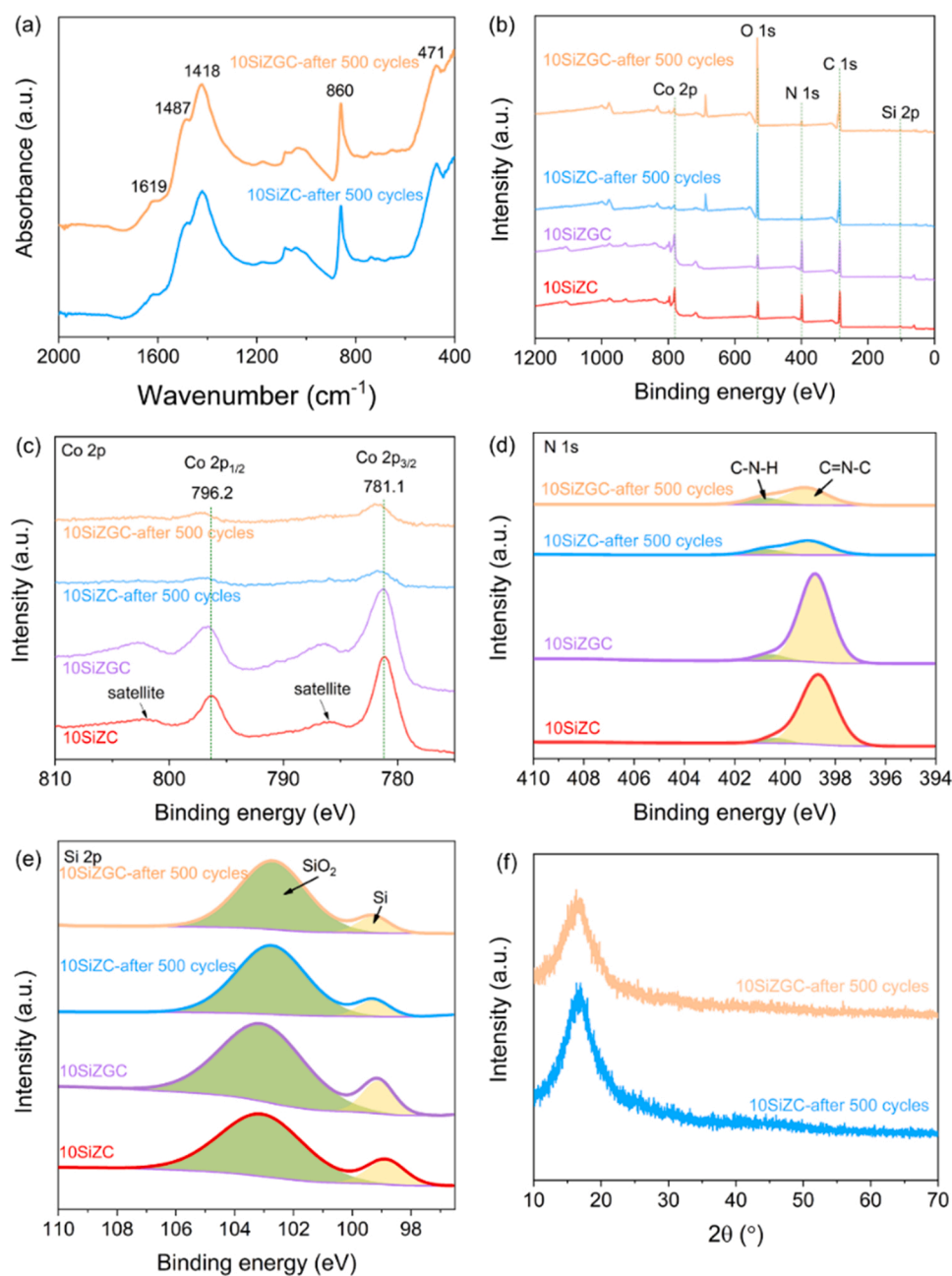
Fig. 4. Structure and phase analyses. (a) FTIR spectra of the 10Si@ZIF composite (10SiZC) and 10Si@ZIF-glass composite (10SiZGC) after cycling, where the number (10) represents that 100-mg Si nanoparticles were added into ZIF-62, accounting for about 10% of the final product by weight. (b)~(e) XPS survey spectra and high-resolution core level of Co 2p, N 1 s, Si 2p spectra for 10SiZC and 10SiZGC before and after cycling, respectively. (f) XRD patterns of 10SiZC and 10SiZGC after 500 cycles.

The above EIS results indicate that both the electron transfer rate and Li^+ diffusion coefficient of 10SiZC and 10SiZGC are greatly enhanced by cycling.

To investigate the structural evolutions of 10SiZC and 10SiZGC after cycling, FTIR spectra were collected. As shown in Fig. 4a, 10SiZC exhibits similar FTIR spectrum to that of 10SiZGC, indicating that both samples have similar structural features after cycling. It is known that the peaks at around 430, 668, 748 and 835 cm^{-1} for the pristine 10SiZC and 10SiZGC (Fig. 2c) are attributed to the Co-N bonds, the ring deformation out-of-plane-bending in the organic ligands, the benzene group of imidazole/benzimidazole, and the in-plane-blending of aromatic ring, respectively [12,21,32]. However, these peaks disappeared in the spectra of the two samples after 500 cycles. This suggests the breakages of the Co-N bonds and rings in the organic ligand after cycling. In addition, the peaks at 471, 860, and 1418 cm^{-1} are ascribed to aromatic C-H bonds, isolated aromatic H vibrations, and ring stretch of organic ligands, respectively [21,33–35], while the peaks at 1487 and 1619 cm^{-1} are attributed to stretching of C-C in the benzimidazole aromatic ring (Fig. 4a) [36].

The surface elemental analyses of 10SiZC and 10SiZGC before and after cycling are carried out by the X-ray photoelectron spectroscopy (XPS) survey spectrum (Fig. 4b), and thereby the existence of Co, N, Si, C and O elements is confirmed, agreeing with the EDS results (Fig. 1). It is seen that the O 1 s signal of the samples after cycling become stronger, and this mainly originate from the SEI (products from electrolyte decomposition). Fig. 4c exhibits the high-resolution spectrum of Co 2p, in which the Co $2p_{1/2}$ and Co $2p_{3/2}$ peaks of both 10SiZC and 10SiZGc samples are located at 796.2 and 781.1 eV with two satellite peaks at 802.1 and 786.0 eV, suggesting the existence of Co^{2+} in both samples. After cycling, these two peaks (796.2 and 781.1 eV) slightly shift to higher binding energy compared with those of pristine samples, implying that the chemical environment of cobalt in 10SiZC and 10SiZGC varies upon insertion/extraction of Li^+ and this could be due to the distortion and local breakage of the Co-N [12]. In Fig. 4d, the peak of N 1 s in the XPS spectrum is deconvoluted into two peaks at 398.7 and 400.4 eV, which are attributed to C=N-C and C-N-H bonds, respectively [12,37]. The fractions of the two bonds are shown in Table S2. 10SiZC shares a similar fraction of the C=N-C bonds (i.e., about 94%) with that in 10SiZGC before cycling. However, the C=N-C bond fractions in both samples dramatically decrease to around 73% after cycling, implying the breakage of C=N-C upon insertion/extraction of Li^+. This agrees well with the FTIR results (Fig. 4a). For the high-resolution XPS spectrum of C 1 s (Fig. S4), the peaks of pristine 10SiZC and 10SiZGC can be deconvoluted into two peaks assigned to C-C/C=C/C-H at 284.8 eV and N=C-N at 286 eV, respectively. In contrast, the C 1 s spectra of 10SiZC and 10SiZGC vary significantly upon cycling, which can be deconvoluted into four peaks. Besides the peak at 284.8 eV, three new peaks appear at 286.6, 288.5, and 290.1 eV, which are related to C-O/N=C-N, O-C=O/C-F, and Li_2CO_3 or lithium alkyl carbonates, respectively, as consequences of both the addition of PVDF as anode binder and the formation of SEI during cycling [12,38–40]. Fig. 4e shows the core level spectra of Si 2p in 10SiZC and 10SiZGC before and after cycles, which exhibit similar characteristics. The peak deconvolution results are shown in Table S3. The XPS peak associated with SiO_2 can be observed in all the composite samples, implying the existence of SiO_2. However, SiO_2 is predominant only in the surface layer ($<$ 5 nm) considering the detection depth limit of XPS. The formation of the thin SiO_2 layer is due to the high tendency of Si to be oxidized when exposed to air, even at room temperature [41]. The existence of SiO_2 was also verified by the FTIR results (Fig. S5). Overall, the fraction of SiO_2 in the as-purchased Si is still much smaller than that of Si. Fig. 4f shows the XRD patterns of 10SiZC and 10SiZGC after 500 cycles. A broad peak at $2\theta \approx 16°$ appears in each pattern, implying the transformation of crystalline ZIF in 10SiZC sample and crystalline Si in both samples into amorphous materials upon cycling.

To detect the morphologies of 10SiZGC and 10SiZC after 500 cycles

at 1 A g^{-1}, SEM and HRTEM measurements were conducted (Fig. 5 and Fig. S6). The overall skeleton of ZIF in 10SiZGC after cycling is preserved and Si particles are still wrapped within ZIF glass, and this is confirmed by the upper right inset, TEM image and EDS mappings in Fig. 5a. The HRTEM image and the selected area electron diffraction (SAED) patterns demonstrate the existence of a large amount of amorphous phase and few crystals with a size of 10~20 nm in 10SiZGC after cycling, as shown in Fig. 5b. The lattice fringes with an interatomic spacing of ~0.31 nm is attributed to Si, implying that the insertion/extraction of Li^+ ions results in the majority of Si in 10SiZGC converting to an amorphous state after 500 cycles. In addition, Fig. S6 shows that the cycled 10SiZC exhibits a similar scenario as 10SiZGC, i.e., a large amount of amorphous phase and few Si crystals, suggesting that not only Si crystals, but also ZIF crystals in 10SiZC transform into amorphous phases upon cycling.

The above results clearly demonstrate the enhanced capacity and rate performance of SiZGC as an anode material for lithium storage [9, 12], and this is achieved by designing and fabricating the Si@ZIF-62 glass composite, in which nano Si is wrapped and protected by porous ZIF glass phase. First, cobalt-ZIF-62 glass possesses an open disordered network structure, which provides more active sites and channels for both storage and transport of Li^+ compared to their crystalline counterparts. Second, the ZIF glass encapsulates Si nano particles to buffer the volume fluctuations of Si during the charging/discharging cycling, thereby realizing excellent cycling performances. In detail, the ZIF glass layer not only stores Li^+ ions, but also suppresses the alloying of Li^+ with wrapped Si to some extent, and also reduces volume change of Si via confinement, and thereby lowers the degree of pulverization of Si in the composite. Even if the wrapped Si nanoparticles are pulverized after cycling (as shown in Scheme 1), a substantial amount of Si is still attached to the inner surface of ZIF glass, and thus the composite structure can remain in a good electrical contact with the copper current collector. Such good contact can facilitate the electron transfer to ensure the alloying process between Li^+ and Si. Third, the insertion/extraction of Li^+ could result in the distortion or breakage of Co-N, and aromatic rings in ZIF, leading to an increase in structural defects and diffusion channels for the transport and storage of Li^+ [12,42]. Moreover, the increased channels lead to more Li^+ ions going into ZIF and reacting with Si, thereby highly enhancing the reversible capacity and rate capability.

4. Conclusions

We designed and fabricated the Si@ZIF-glass composite compromising interior high-capacity Si nano particles and exterior ZIF glass phase for lithium storage, which yields a strong synergistic effect. Such a unique architecture in ZIF glass buffers the volume changes of Si and thus prevents its pulverization, and hence promotes the transport kinetics for both electrons and lithium ions. In addition, ZIF glass itself also enhanced the electrochemical performance of Si@ZIF-glass based anode owing to its open network structure that facilitates the Li^+ ion diffusion and storage. As a consequence, 10SiZGC based anode exhibits the capacity of 650 mA h g^{-1}, which is about three times and six times as high as that of ZIF glass and ZIF crystal at the current density of 1 A g^{-1} after 500 cycles, respectively. Our findings paved a new avenue for developing anode material for the next generation of high-performance LIBs. Moreover, our approach to construct hierarchical Si@ZIF-glass composite could be further extended to other types of ZIF glasses to combine with highly active materials like Sn and SnO_2 for application in electrochemical energy storage.

CRediT authorship contribution statement

Jiajia Yan: Conceptualization, Methodology, Investigation, Data curation, Writing – original draft. **Chengwei Gao**: Conceptualization, Methodology, Data curation, Writing – review & editing. **Shibin Qi**: Data curation, Validation. **Zhenjing Jiang**: Data curation. **Lars**
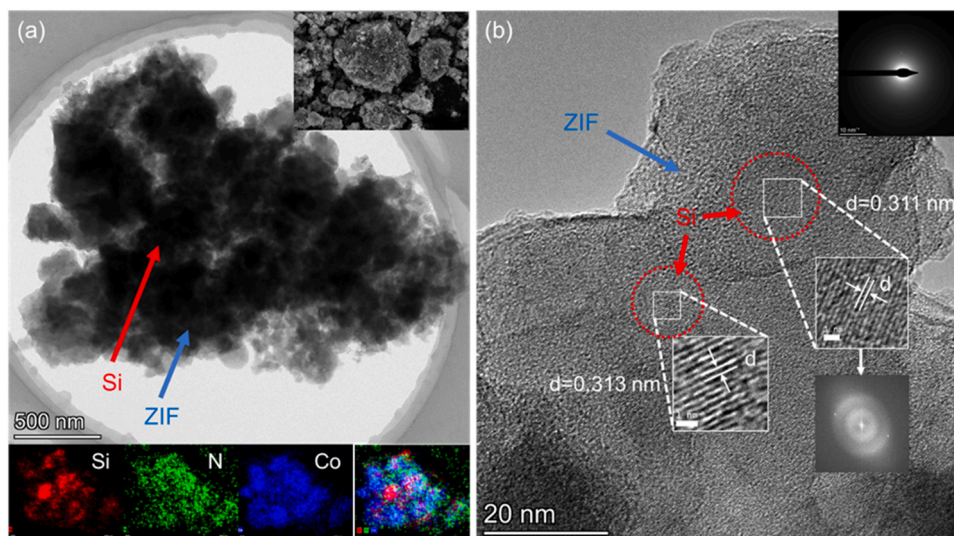
Fig. 5. Microscopic characterization. (a) SEM image (the upper right inset), TEM image and EDS mappings of Si, N, Co for 10SiZGC after cycling. (b) HRTEM image and the corresponding SAED patterns of 10SiZGC after cycling.

Rosgaard Jensen: Data curation. **Hongbing Zhan**: Data curation. **Yanfei Zhang**: Data curation, Supervision, Writing – review & editing. **Yuanzheng Yue**: Conceptualization, Project administration, Supervision, Writing – review & editing.

Declaration of Competing Interest

The authors declare that they have no known competing financial interests or personal relationships that could have appeared to influence the work reported in this paper.

Data availability

Data will be made available on request.

Acknowledgments

Appendix A. Supporting information

Supplementary data associated with this article can be found in the online version at doi:10.1016/j.nanoen.2022.107779.

References

[1] S. Chae, S.H. Choi, N. Kim, J. Sung, J. Cho, Integration of graphite and silicon anodes for the commercialization of high-energy lithium-ion batteries, Angew. Chem. Int. Ed. 59 (1) (2020) 110–135, https://doi.org/10.1002/anie.201902085.

[2] Y. Zhang, J. Ren, T. Xu, A. Feng, K. Hu, N. Yu, Y. Xia, Y. Zhu, Z. Huang, G. Wu, Covalent bonding of Si nanoparticles on graphite nanosheets as anodes for lithium-ion batteries using diazonium chemistry, Nanomaterials 9 (12) (2019) 1741, https://doi.org/10.3390/nano9121741.

[3] Y. Xu, Y. Zhu, C. Wang, Mesoporous carbon/silicon composite anodes with enhanced performance for lithium-ion batteries, J. Mater. Chem. A 2 (25) (2014) 9751–9757, https://doi.org/10.1039/c4ta01691b.

[4] D.H.S. Tan, Y.-T. Chen, H. Yang, W. Bao, B. Sreenarayanan, J.-M. Doux, W. Li, B. Lu, S.-Y. Ham, B. Sayahpour, J. Scharf, E. A.Wu, G. Deysher, H.E. Han, H.J. Hah, H. Jeong, J.B. Lee, Z. Chen, Y.S. Meng, Carbon-free high-loading silicon anodes enabled by sulfide solid electrolytes, Science 373 (2021) 1494–1499, https://doi.org/10.1126/science.abg7217.

[5] Y. Ding, Z.P. Cano, A. Yu, J. Lu, Z. Chen, Automotive Li-ion batteries: current status and future perspectives, Electrochem. Energy Rev. 2 (1) (2019) 1–28, https://doi.org/10.1007/s41918-018-0022-z.

[6] F. Chen, J. Han, D. Kong, Y. Yuan, J. Xiao, S. Wu, D.-M. Tang, Y. Deng, W. Lv, J. Lu, F. Kang, Q.-H. Yang, 1000 Wh L−1 lithium-ion batteries enabled by crosslink-shrunk tough carbon encapsulated silicon microparticle anodes, Natl. Sci. Rev. 8 (9) (2021), https://doi.org/10.1093/nsr/nwab012.

[7] A. Magasinski, P. Dixon, B. Hertzberg, A. Kvit, J. Ayala, G. Yushin, High-performance lithium-ion anodes using a hierarchical bottom-up approach, Nat. Mater. 9 (4) (2010) 353–358, https://doi.org/10.1038/nmat2725.

[8] M. Ko, S. Chae, J. Ma, N. Kim, H.-W. Lee, Y. Cui, J. Cho, Scalable synthesis of silicon-nanolayer-embedded graphite for high-energy lithium-ion batteries, Nat. Energy 1 (9) (2016) 1–8, https://doi.org/10.1038/nenergy.2016.113.

[9] C. Gao, P. Wang, Z. Wang, S.K. Kær, Y. Zhang, Y. Yue, The disordering-enhanced performances of the Al-MOF/graphene composite anodes for lithium ion batteries, Nano Energy 65 (2019), 104032, https://doi.org/10.1016/j.nanoen.2019.104032.

[10] X. Li, F. Cheng, S. Zhang, J. Chen, Shape-controlled synthesis and lithium-storage study of metal-organic frameworks Zn₄O (1, 3, 5-benzenetribenzoate) 2, J. Power Sources 160 (1) (2006) 542–547, https://doi.org/10.1016/j.jpowsour.2006.01.015.

[11] T. Wei, M. Zhang, P. Wu, Y.-J. Tang, S.-L. Li, F.-C. Shen, X.-L. Wang, X.-P. Zhou, Y.-Q. Lan, POM-based metal-organic framework/reduced graphene oxide nanocomposites with hybrid behavior of battery-supercapacitor for superior lithium storage, Nano Energy 34 (2017) 205–214, https://doi.org/10.1016/j.nanoen.2017.02.028.

[12] C. Gao, Z. Jiang, S. Qi, P. Wang, L.R. Jensen, M. Johansen, C.K. Christensen, Y. Zhang, D.B. Ravnsbæk, Y. Yue, Metal-organic framework glass anode with an exceptional cycling-induced capacity enhancement for lithium-ion batteries, Adv. Mater. 34 (10) (2022), 2110048, https://doi.org/10.1002/adma.202110048.

[13] Y. Han, P. Qi, X. Feng, S. Li, X. Fu, H. Li, Y. Chen, J. Zhou, X. Li, B. Wang, In situ growth of MOFs on the surface of si nanoparticles for highly efficient lithium storage: Si@MOF nanocomposites as anode materials for lithium-ion batteries, ACS Appl. Mater. Interfaces 7 (4) (2015) 2178–2182, https://doi.org/10.1021/am5081937.

[14] Y. Bai, M. Zeng, X. Wu, Y.Q. Zhang, J.W. Wen, J. Li, Three-dimensional cage-like Si@ZIF-67 core-shell composites for high-performance lithium storage, Appl. Surf. Sci. 510 (2020), https://doi.org/10.1016/j.apsusc.2020.145477.

[15] Q. Wei, Y.M. Chen, X.J. Hong, C.L. Song, Y. Yang, L.P. Si, M. Zhang, Y.P. Cai, Saclike-silicon nanoparticles anchored in ZIF-8 derived spongy matrix as high-performance anode for lithium-ion batteries, J. Colloid Interface Sci. 565 (2020) 315–325, https://doi.org/10.1016/j.jcis.2020.01.050.

[16] Q. Wei, Y.M. Chen, X.J. Hong, C.L. Song, Y. Yang, L.P. Si, M. Zhang, Y.P. Cai, Novel bread-like nitrogen-doped carbon anchored nano-silicon as high-stable anode for lithium-ion batteries, Appl. Surf. Sci. 511 (2020), https://doi.org/10.1016/j.apsusc.2020.145609.

[17] L. Longley, S.M. Collins, C. Zhou, G.J. Smales, S.E. Norman, N.J. Brownbill, C.W. Ashling, P.A. Chater, R. Tovey, C.-B. Schönlieb, Liquid phase blending of metal-organic frameworks, Nat. Commun. 9 (1) (2018) 1–10, https://doi.org/10.1038/s41467-018-04553-6.

[18] L. Frentzel-Beyme, M. Kloß, R. Pallach, S. Salamon, H. Moldenhauer, J. Landers, H. Wende, J. Debus, S. Henke, Porous purple glass – a cobalt imidazolate glass with accessible porosity from a meltable cobalt imidazolate framework, J. Mater. Chem. A 7 (3) (2019) 985–990, https://doi.org/10.1039/c8ta08016j.

[19] A. Qiao, T.D. Bennett, H. Tao, A. Krajnc, G. Mali, C.M. Doherty, A.W. Thornton, J. C. Mauro, G.N. Greaves, Y. Yue, A metal–organic framework with ultrahigh glass-forming ability, Sci. Adv. 4 (3) (2018) eaao6827, https://doi.org/10.1126/sciadv. aao6827.

[20] R. Banerjee, A. Phan, B. Wang, C. Knobler, H. Furukawa, M. O'Keeffe, O.M. Yaghi, High-throughput synthesis of zeolitic imidazolate frameworks and application to CO_2 capture, Science 319 (5865) (2008) 939–943, https://doi.org/10.1126/science.1152516.

[21] A. Ulu, Metal–organic frameworks (MOFs): a novel support platform for ASNase immobilization, J. Mater. Sci. 55 (14) (2020) 6130–6144, https://doi.org/10.1007/s10853-020-04452-6.

[22] M. Mubashir, R. Ashena, A. Bokhari, A. Mukhtar, S. Saqib, A. Ali, R. Saidur, K. S. Khoo, H.S. Ng, F. Karimi, Effect of process parameters over carbon-based ZIF-62 nano-rooted membrane for environmental pollutants separation, Chemosphere 291 (2022), 133006, https://doi.org/10.1016/j.chemosphere.2021.133006.

[23] S. Mala, L. Tsybeskov, D. Lockwood, X. Wu, J.-M. Baribeau, Raman scattering in Si/SiGe nanostructures: revealing chemical composition, strain, intermixing, and heat dissipation, J. Appl. Phys. 116 (1) (2014), 014305, https://doi.org/10.1063/1.4886598.

[24] S. Ashraf, R. Mehek, N. Iqbal, T. Noor, G. Ali, A. Wahab, A.A. Qayyum, A. Ahmad, ZIF 67 derived Co–Sn composites with N-doped nanoporous carbon as anode material for Li-ion batteries, Mater. Chem. Phys. 270 (2021), 124824, https://doi.org/10.1016/j.matchemphys.2021.124824.

[25] Y. Liu, X. Que, X. Wu, Q. Yuan, H. Wang, J. Wu, Y. Gui, W. Gan, ZIF-67 derived carbon wrapped discontinuous CoxP nanotube as anode material in high-performance Li-ion battery, Mater. Today Chem. 17 (2020), 100284, https://doi.org/10.1016/j.mtchem.2020.100284.

[26] C. Li, X. Lou, Q. Yang, X. Zou, B. Hu, Remarkable improvement in the lithium storage property of Co_2 $(OH)_2BDC$ MOF by covalent stitching to graphene and the redox chemistry boosted by delocalized electron spins, Chem. Eng. J. 326 (2017) 1000–1008, https://doi.org/10.1016/j.cej.2017.06.048.

[27] B. Li, F. Yao, J.J. Bae, J. Chang, M.R. Zamfir, D.T. Le, D.T. Pham, H. Yue, Y.H. Lee, Hollow carbon nanospheres/silicon/alumina core-shell film as an anode for lithium-ion batteries, Sci. Rep. 5 (2015) 7659, https://doi.org/10.1038/srep07659.

[28] W. An, B. Gao, S. Mei, B. Xiang, J. Fu, L. Wang, Q. Zhang, P.K. Chu, K. Huo, Scalable synthesis of ant-nest-like bulk porous silicon for high-performance lithium-ion battery anodes, Nat. Commun. 10 (1) (2019) 1–11, https://doi.org/10.1038/s41467-019-09510-5.

[29] X. Hu, J. Jia, G. Wang, J. Chen, H. Zhan, Z. Wen, Reliable and general route to inverse opal structured nanohybrids of carbon-confined transition metal sulfides quantum dots for high-performance sodium storage, Adv. Energy Mater. 8 (25) (2018), 1801452, https://doi.org/10.1002/aenm.201801452.

[30] Y. Yu, C. Yue, X. Lin, S. Sun, J. Gu, X. He, C. Zhang, W. Lin, D. Lin, X. Liao, ZIF-8 cooperating in TiN/Ti/Si nanorods as efficient anodes in micro-lithium-ion-batteries, ACS Appl. Mater. Interfaces 8 (6) (2016) 3992–3999, https://doi.org/10.1021/acsami.5b11287.

[31] X.L. Wu, Y.G. Guo, J. Su, J.W. Xiong, Y.L. Zhang, L.J. Wan, Carbon-nanotube-decorated nano-LiFePO4@C cathode material with superior high-rate and low-temperature performances for lithium-ion batteries, Adv. Energy Mater. 3 (9) (2013) 1155–1160, https://doi.org/10.1002/aenm.201300159.

[32] G. Khandelwal, N.P.M.J. Raj, S.-J. Kim, ZIF-62: a mixed linker metal–organic framework for triboelectric nanogenerators, J. Mater. Chem. A 8 (34) (2020) 17817–17825, https://doi.org/10.1039/D0TA05067A.

[33] Y. Chen, C. Zou, M. Mastalerz, S. Hu, C. Gasaway, X. Tao, Applications of micro-fourier transform infrared spectroscopy (FTIR) in the geological sciences—a review, Int. J. Mol. Sci. 16 (12) (2015) 30223–30250, https://doi.org/10.3390/ijms161226227.

[34] M. Mubashir, Y.F. Yeong, K.K. Lau, T.L. Chew, J. Norwahyu, Efficient CO_2/N_2 and CO_2/CH_4 separation using NH_2-MIL-53 (Al)/cellulose acetate (CA) mixed matrix membranes, Sep. Purif. Technol. 199 (2018) 140–151, https://doi.org/10.1016/j.seppur.2018.01.038.

[35] D. Tuncel, A. Ökte, Improved adsorption capacity and photoactivity of ZnO-ZIF-8 nanocomposites, Catal. Today 361 (2021) 191–197, https://doi.org/10.1016/j.cattod.2020.04.014.

[36] J. Cheng, D. Ma, S. Li, W. Qu, D. Wang, Preparation of zeolitic imidazolate frameworks and their application as flame retardant and smoke suppression agent for rigid polyurethane foams, Polymers 12 (2) (2020) 347, https://doi.org/10.3390/polym12020347.

[37] C. Hu, Y.-C. Huang, A.-L. Chang, M. Nomura, Amine functionalized ZIF-8 as a visible-light-driven photocatalyst for Cr (VI) reduction, J. Colloid Interface Sci. 553 (2019) 372–381, https://doi.org/10.1016/j.jcis.2019.06.040.

[38] I. Muzammil, Y. Li, M. Lei, Tunable wettability and pH-responsiveness of plasma copolymers of acrylic acid and octafluorocyclobutane, Plasma Process. Polym. 14 (10) (2017), 1700053, https://doi.org/10.1002/ppap.201700053.

[39] X. Chen, X. Wang, D. Fang, A review on C1s XPS-spectra for some kinds of carbon materials, Fuller., Nanotub. Carbon Nanostruct. 28 (12) (2020) 1048–1058, https://doi.org/10.1080/1536383X.2020.1794851.

[40] S. Jurng, Z.L. Brown, J. Kim, B.L. Lucht, Effect of electrolyte on the nanostructure of the solid electrolyte interphase (SEI) and performance of lithium metal anodes, Energy Environ. Sci. 11 (9) (2018) 2600–2608, https://doi.org/10.1039/C8EE00364E.

[41] M. Morita, T. Ohmi, E. Hasegawa, M. Kawakami, M. Ohwadab, Growth of native oxide on a silicon surface, J. Appl. Phys. 68 (3) (1990) 1272–1281, https://doi.org/10.1063/1.347181.

[42] Y. Lin, Q. Zhang, C. Zhao, H. Li, C. Kong, C. Shen, L. Chen, An exceptionally stable functionalized metal–organic framework for lithium storage, Chem. Commun. 51 (4) (2015) 697–699, https://doi.org/10.1039/C4CC07149B.